Dynamic estimation of three-dimensional cerebrovascular deformation from rotational angiography

Chong Zhang,[1,a)] Maria-Cruz Villa-Uriol,[1] Mathieu De Craene,[1] José María Pozo,[1] Juan M. Macho,[2] and Alejandro F. Frangi[3,b)]

[1)] *Center for Computational Imaging & Simulation Technologies in Biomedicine (CISTIB) - Universitat Pompeu Fabra (UPF), Networking Biomedical Research Center on Bioengineering, Biomaterials and Nanomedicine (CIBER-BBN), Barcelona, Spain*

[2)] *Department of Vascular Radiology, Hospital Clinic i Provincial de Barcelona, Spain*

[3)] *Center for Computational Imaging & Simulation Technologies in Biomedicine (CISTIB) - Universitat Pompeu Fabra (UPF), Networking Biomedical Research Center on Bioengineering, Biomaterials and Nanomedicine (CIBER-BBN), and Institució Catalana de Recerca i Estudis Avançats (ICREA), Barcelona, Spain*

(Dated: 7 January 2011)

Purpose: The objective of this study is to investigate the feasibility of detecting and quantifying 3D cerebrovascular wall motion from a single 3D rotational X-ray angiography (3DRA) acquisition within a clinically acceptable time, and computing from the estimated motion field for the further biomechanical modeling of the cerebrovascular wall.

Methods: The whole motion cycle of the cerebral vasculature is modeled using a 4D B-spline transformation, which is estimated from a 4D to 2D+t image registration framework. The registration is performed by optimizing a single similarity metric between the entire 2D+t measured projection sequence and the corresponding forward projections of the deformed volume at their exact time instants. The joint use of two acceleration strategies together with their implementation on graphics processing units are also proposed so as to reach computation times close to clinical requirements. For further characterizing vessel wall properties, an approximation of the wall thickness changes is obtained through a strain calculation.

Results: Evaluation on *in silico* and *in vitro* pulsating phantom aneurysms demonstrated an accurate estimation of wall motion curves. In general, the error was below 10% of the maximum pulsation, even in the situation when substantial inhomogeneous intensity pattern was present. Experiments on *in vivo* data provided realistic aneurysm and vessel wall motion estimates, whereas in regions where motion was neither visible nor anatomically possible no motion was detected. The use of the acceleration strategies enabled completing the estimation process for one entire cycle in 5-10 minutes without degrading the overall performance. The strain map extracted from our motion estimation provided a realistic deformation measure of the vessel wall.

Conclusions: Our technique has demonstrated that it can provide accurate and robust 4D estimates of cerebrovascular wall motion within a clinically acceptable time, **although it has to be applied to a larger patient population prior to possible wide application to routine endovascular procedures.** In particular, for the first time, this feasibility study has shown that *in vivo* cerebrovascular motion can be obtained intra-procedurally from a 3DRA acquisition. Results have also shown the potential of performing strain analysis using this imaging modality, making thus possible for the future modeling of biomechanical properties of the vascular wall.

Keywords: cerebral vasculature; image registration; motion estimation; rotational angiography

[a]Electronic mail: chong.zhang@upf.edu

[b]Electronic mail: alejandro.frangi@upf.edu

I. INTRODUCTION

Cerebrovascular diseases in general cause changes to the architecture of blood vessels in the brain by making them narrow, stiff, deformed, or uneven. The pathogenesis of these diseases is believed to be dependent on the complex interactions among multiple physiological and mechanical factors such as hemodynamics, wall biomechanics and mechanobiology[1]. Unfortunately, patient-specific vessel wall properties cannot be measured *in vivo* with current medical imaging techniques[2]. In many situations, an inverse problem approach based on a mathematical model for the biomechanics of the vasculature is a valid surrogate to estimate material and structural parameters[3,4]. An example of such approach consists of determining these unknown parameters by applying known boundary conditions on the vessel wall and analyzing its mechanical responses such as vascular wall motion. Tracking this motion should also allow embedding wall compliance as a boundary condition for hemodynamic simulations[5]. Besides, other studies suggest that even the direct visualization of wall motion abnormalities may be helpful for analyzing pathological features of the cerebral vasculature[6,7]. Therefore, quantifying vascular wall motion and deformation has the potential of impacting treatment selection and preoperative planning of cerebrovascular diseases. However, since such motion is in general expected to be in a sub-millimeter range[7–9], it represents a challenge in terms of the available image resolution of current clinical imaging techniques.

Various techniques have been proposed for estimating motion or reconstructing dynamic 3D structures using projection images acquired from image modalities like three-dimensional rotational X-ray angiography (3DRA) and cone beam computed tomography (CBCT). ECG-gated techniques[10–12] constitute the most typical approach, where a reduced set of projections linked to a particular cardiac phase is used to reconstruct a volumetric image using iterative[13] or analytical[11,14] reconstruction methods. Recently, a technique[15] has been proposed to incorporate a 4D motion estimation into a projection motion-compensated 3D reconstruction process by comparing the latter to an initial reference reconstruction. However, the estimated motion could be limited by the 3D reconstruction error even before performing the 3D/3D registration. In other works[16,17], continuous respiratory motion during a CBCT acquisition has been estimated by optimizing the similarity between the measured and the corresponding views of a deforming reference volume obtained from CT. However, their techniques need additional motion constraints such as a prior motion model or a regularization term. Also, their need of two acquisitions increases patient exposure to radiation, limiting their clinical applicability.

We aim to retrieve the dynamic 3D morphology of a structure of interest from a single 3DRA acquisition (e.g. cerebral aneurysm or a vessel segment). 3DRA is routinely performed in clinical practice during endovascular interventions. One standard acquisition provides a sequence of 2D rotational X-ray angiographies and an isotropic high-resolution 3D volumetric image reconstructed from them. A physiological signal synchronized with the projections can also be recorded. In a previous work[18], we proposed a method to estimate the 3D morphology of the structure of interest at a given time instant by registering forward projections of the deformed 3DRA volume to a sparse set of 2D measured projections through a temporal weighting scheme. However, since this technique only represents the spatiotemporal motion through independent 3D morphology estimation at discrete time points, it fails to address the intrinsic temporal consistency or continuity of motion. In addition, the estimated morphology can be compromised by the residual motion introduced by forcing the forward projections at a specific time instant to match the measured projections in its temporal vicinity. In general, this problem is also common for ECG-gated methods.

In this paper, instead of representing the motion over time by independent 3D transformations as proposed in[18], we employ a single 4D B-spline transformation model for the whole motion cycle. It is estimated from a 4D to 2D+t image registration framework. The basic idea of the transformation model is to deform an object by manipulating an underlying mesh of control points, resulting in a smooth and continuous deformation of the reference image at any time of the motion cycle. Thus, an estimate of arbitrarily small displacement or deformation can be achieved through the interpolation from the movements of the control points. Meanwhile, the registration is optimized by measuring a single similarity metric between the entire measured projection sequence and the corresponding forward projections of the deformed volume at their corresponding exact time instants. This improves the temporal consistency without introducing blurring, as well as the robustness to image noise and artifacts such as contrast agent induced intensity inhomogeneity. Performing the motion estimation from the projection space improves the accuracy of the motion estimate as the pixel resolution is higher in the 2D+t measured projections than in the 3D image. On the other hand, computational cost is high for the simultaneous processing of such high-resolution temporal sequences of 3D images, 2D measured and forward projections. We therefore introduce the joint use of two acceleration strategies: a precomputation at the forward projection generation stage and an object-adaptive region-of-interest (ROI) for the forward projection update and the metric computation. Since less data have to be processed, these strategies also result in a reduction of memory requirements. Preliminary results and the overall registration framework were previously published as in[19]. Here a detailed method description is presented, with the integration of the acceleration strategies implemented on graphics processing units (GPU)[20]. An extended validation is performed on *in silico*, *in vitro* phantoms, and for the first time, on *in vivo* patient data. In this paper, we also explore whether strain as estimated from the motion field from imaging data can be applied to the personalization of modeling of the vascular wall biomechanical properties.

II. MATERIAL AND METHODS

II.A. Motion estimation algorithm

The motion estimation algorithm presented in this paper consists of three steps. First, in order to overcome the limited spatial coverage from each of the separate motion cycles, the measured projections are reordered and built into one canonical motion cycle, according to a synchronized physiological signal such as ECG. Second, a 4D-to-2D+t image registration is performed to obtain a single spatiotemporal transformation field over the whole canonical motion cycle. Third, after obtaining the optimal transformation parameter, instantaneous 3D images of the analyzed morphology at any desired time instant can be extracted by applying the 4D transformation to the reference volume image.

II.A.1. Canonical motion cycle

During the rotational run, the total angular coverage of the measured projections for one cardiac or motion cycle is 40-50°. Such viewing range may not be informative about the 3D motion along certain directions. This drawback could be potentially compensated for by providing an a priori motion model as in[17]. An alternative is to add a pseudo-periodicity constraint term to the optimization function as in[16]. However, the optimization process is complicated by the need of determining empirically the weight for such regularization.

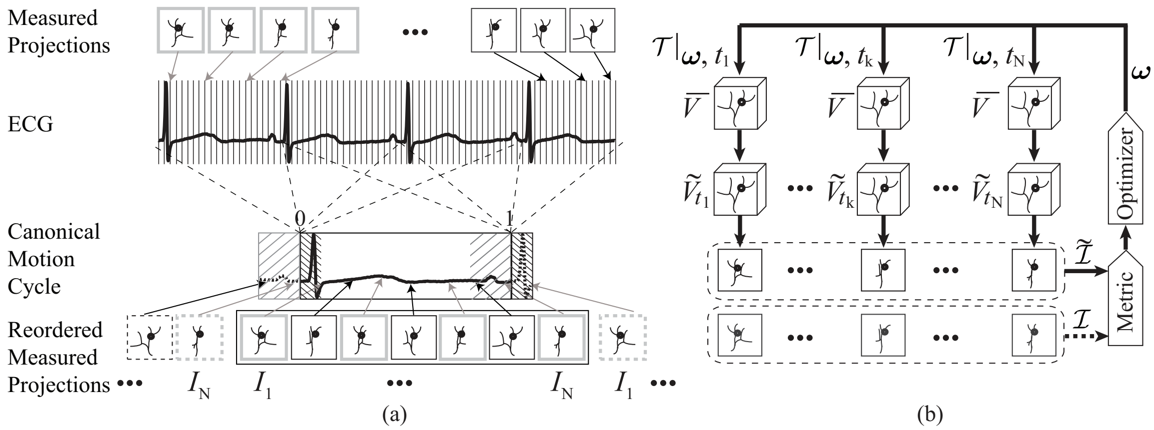

FIG. 1. (a) Each motion cycle in the N measured projections sequence is normalized to have a unitary duration, according to a physiological signal such as ECG. And the time for each projection is normalized to the full length of its corresponding cardiac cycle. Thus all projections fall within a $[0, 1)$ interval. A reordered measured projections sequence can then be obtained based on this normalized time to form one canonical motion cycle. (b) An overview of the 4D-to-2D+t image registration framework, where one metric measuring the similarity between the measured and forward projection sequences, $\mathcal{I}$ and $\tilde{\mathcal{I}}$, is used to estimate a 4D continuous and smooth transformation model parameterized according to $\boldsymbol{\omega}$ over space and time.

We overcome this limitation by reordering all the projections (spanning 4-5 cardiac cycles) to build one canonical motion cycle. This step is carried out as described in[18] and as illustrated in Fig. 1(a). We first normalize the period of each cycle to have a unitary duration according to a physiological signal such as ECG, which is recorded synchronously together with the projections. The time for each of the N measured projections is normalized to the full length of its corresponding cardiac cycle. Hence, all projections fall within the $[0, 1)$ interval and are then sorted by this normalized time to build one canonical motion cycle as $\mathcal{I} = \{I_{t_k}(\mathbf{x}) \mid k = 1 \ldots N\}$, where $I_{t_k}(\mathbf{x})$ represents the measured projection and at the normalized time t_k ($0 \leq t_k \leq t_{k+1} < 1$). In practice, images acquired at similar cardiac phases in the canonical cycle are approximately separated by a 40-50° angular shift per cycle. By the use of this compounding strategy, the projection spatial viewing angle range is enriched at any temporal vicinity. In addition, the temporal resolution can be considered to be approximately increased by a factor corresponding to the number of cycles during the acquisition.

II.A.2. *4D-to-2D+t image registration*

The entire measured projection sequence is simultaneously processed to estimate a 4D continuous and smooth transformation model parameterized over space and time. A single metric captures the similarity between projection sequences instead of considering separate similarities between individual projections.

As shown in Fig. 1(b), motion throughout the canonical cycle is represented by a transformation $\mathcal{T}$ parameterized by $\boldsymbol{\omega}$. Thus, the 3D instantaneous motion at time t is given by deforming a reference volumetric image $\overline{V}$:

$$\widetilde{V}_t(\mathbf{p}) = \overline{V}(\mathcal{T}(\boldsymbol{\omega}, \mathbf{p}, t)), \tag{1}$$

where $\mathbf{p}$ is a point in $\widetilde{V}_t$. In this paper, a B-spline based transformation[21,22] is used. The displacement of $\mathbf{p}$ is represented by a 4D tensor product of cubic B-spline functions (i.e. $\beta(\cdot)$ in the temporal dimension and $B(\cdot)$ the 3D tensor of $\beta(\cdot)$ in the spatial dimensions), defined on a sparse control points grid $(\mathbf{p_c}, t_\tau)$:

$$\mathcal{T}(\boldsymbol{\omega}, \mathbf{p}, t) = \mathbf{p} + \sum_{\tau,\mathbf{c}} \beta\left(\frac{t - t_\tau}{\Delta_\tau}\right) B\left(\frac{\mathbf{p} - \mathbf{p_c}}{\boldsymbol{\Delta}_\mathbf{c}}\right) \boldsymbol{\omega}_{\tau,\mathbf{c}}, \tag{2}$$

where $\boldsymbol{\omega}$ is an array of the control grid coefficients, acting as parameters of the B-spline, $\mathbf{c}$ the spatial index and τ the temporal index, $(\boldsymbol{\Delta}_\mathbf{c}, \Delta_\tau)$ the width of the functions in each dimension. This transformation model ensures both temporal and spatial consistency and smoothness without compromising the local motion recovery due to its local control property. More importantly, an estimate of small displacement or deformation can be achieved through the underlying interpolation between the control points. Note that to keep the continuity at both ends of the cycle ($t_{\tau_{min}} = 0$ and $t_{\tau_{max}} = 1$), we need to impose a pseudo-cyclic condition $\boldsymbol{\omega}_{\tau_{min},\mathbf{c}} = \boldsymbol{\omega}_{\tau_{max},\mathbf{c}}$. A simple implementation is to extend the range of the transformation model on the temporal axis at both ends, as illustrated in Fig. 1(a).

For each I_{t_k}, a corresponding digitally reconstructed radiograph (DRR), $\tilde{I}_{t_k}$, is calculated to simulate the X-ray angiography through a ray casting process[23]. For the rotational angiography (RA) sequence, their projection geometry is known for each projection, including the X-ray source position, the projection detector position, and the rotational orientation. We denote by $\tilde{\mathcal{I}}$ the entire DRR sequence, which is iteratively modified to match the measured projection sequence $\mathcal{I}$ for an optimal estimation of $\hat{\boldsymbol{\omega}}$:

$$\hat{\boldsymbol{\omega}}=\underset{\boldsymbol{\omega}}{\operatorname{argmin}}\left\{M(\boldsymbol{\omega},\mathcal{I},\tilde{\mathcal{I}})\right\}, \tag{3}$$

where M is the similarity metric between two mapping regions. Mutual information[24,25] was used as the metric. Since the registration matches simultaneously all the projections, sampled points from the entire sequence are considered as within one region, forming a single histogram. Therefore, instead of having one independent metric for each projection pair, M describes the similarity between the two sequences $\mathcal{I}$ and $\tilde{\mathcal{I}}$. Histograms are approximated using Parzen windows for the probability calculation[26]. The use of one metric measuring the similarity between projection sequences makes the registration more robust against local intensity variations (e.g noise and inhomogeneous contrast mixing) than considering similarities between individual projections separately. Note that due to the higher spatial resolution in measured projections compared to the volumetric image, performing the motion estimation from the projection space improves spatial accuracy of the recovered motion field. In our case, a displacement equivalent to one pixel translates into approximately 0.3 voxel. The L-BFGS-B algorithm[27] is used as the optimizer, due to its ability in handling a very large number of parameters.

II.B. An efficient implementation

Dealing simultaneously with such high-resolution 4D image, 2D measured projections and DRRs, requires excessive memory and long computation time. For the method to be practically applicable, reducing both of them without degrading the performance is desirable. Two strategies are jointly used in order to process the data of interest at each iteration during the registration process. The fact that both computation and memory costs scale with the amount of processed data makes these strategies efficient. They are further implemented on GPU so as to facilitate the clinical use of our technique at a reasonable execution time. The main idea of the GPU implementation method is summarized in Appendix and a detailed description can be found in[20].

II.B.1. DRRs precomputation

In 3DRA images, the structure of interest (e.g. an aneurysm or a vessel segment) is in the order of millimeters, occupying a reduced region in the image (see an example in Fig. 2(a)). Thus, during the motion estimation process, the transformation can be applied only to a volume of interest (VOI) while the rest of the volume remains unmodified. Provided that the actual motion present outside the VOI is smaller than or of the same magnitude as the motion in the VOI, it will not affect significantly the estimated motion. The reason is that due to the use of a sparse B-spline **control-points grid**, any motion outside may only influence one projection in a particular direction while the motion of each control point is the result of several projections. However, in order to simulate realistic X-ray projections, voxels of the entire volume must be integrated at each iteration to update the DRRs. In order to avoid redundant computation, for each pixel $\mathbf{x}$, the corresponding ray is split into two parts: inside and outside the VOI. The constant outside part is precomputed, and at each iteration only the inside part is integrated and updated to the sum of both parts. An illustration is shown in Fig. 2(a) for a VOI containing an aneurysm. The speedup factor using such pre-computation is the ratio between the ray segment length crossing the entire volume and that of the VOI. The memory reduction rate is also expected to scale with this factor.

II.B.2. Object-adaptive region-of-interests

A common approach to accelerate the metric computation is to subsample the images. Uniform subsampling is not the most efficient method, and special attention should be paid to reduce the calculation of the metric and its derivatives by sampling, for example the object of interest[28] or its edges[29]. We follow this strategy by encouraging dense sampling of image regions that strongly influence the metric. Since morphology changes of the aneurysm or vessel wall are reflected on the contrast enhanced lumen boundaries, two object-adaptive sampling regions are introduced: the projected object ($\mathrm{S_{OR}}$) and the projected boundary ($\mathrm{S_{BR}}$). Consequently, the typical projected VOI, denoted as $\mathrm{S_{VR}}$, for the computation of the metric are replaced by the sequences of pixels from the sampling regions $\mathrm{S_{OR}}$ or $\mathrm{S_{BR}}$. An illustration of these regions is shown in Fig. 2.

There are many techniques automatically delineate such regions. Note that the accurate definition of the sampling regions in 2D is not crucial for our method, as our interest is to quantify 3D morphological changes. And since a reference image is available in 3D, we first obtain one approximated 3D shape of the region using a threshold-based method, and then define the region by simply projecting it on each projection. A unique property of a 3DRA volume is that, looking at the histogram of this 3D image, there is a sharp differentiation of the contrast agent (CA) filled regions (i.e. aneurysms and vessels) from the background. This results in clearly separated classes with the CA filled regions mapped to high voxel value range and the background to low voxel value range[10,30]. Meanwhile, on the contrast filled boundaries in the projection images, in general a region of progressive intensity change exists. This is mainly due to the changes in length of the X-ray traversing the contrast-filled region on the boundaries, resulting in a continuous change of the accumulated attenuation. Consequently, this results in a similar pattern in the 3D reconstructed volume. Based on this observation, the S_{OR} is calculated for each projection as follows. First, a boundary value of the studied object is selected by identifying the CA filled regions from the histogram. Second, on the corresponding ray for a specific pixel, as long as there is one sampled point having larger intensity than this boundary value, the pixel is considered to be part of the S_{OR}. The obtained region is comparable to the projected "shadow" of a 3D object from thresholding. Similarly for the S_{BR}, we first obtain two of these regions from different threshold values, by repeating the process of the S_{OR} region for two thresholds. One overestimates (i.e. higher threshold) and the other underestimates (i.e. lower thresholds) the contrast filling region. The S_{BR} region is obtained by subtraction of the two resulting regions. These boundary identifying values or thresholds in the histogram can be obtained empirically or using e.g. Otsu's method[31]. Note that this gradually changing intensity pattern on the boundaries between the contrast-filled region and the background also helps the recovery of a subvoxel displacement estimated through the deformation of the reference image. The reason is that such an intensity function follows a smooth transition that gives information on the boundaries at a finer scale than the voxel grid, i.e. subvoxel resolution.

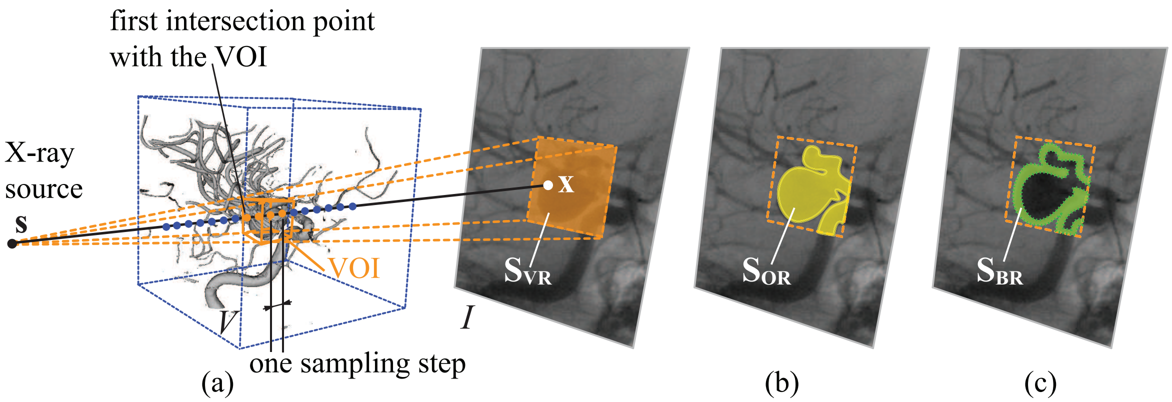

FIG. 2. (a) An illustration of the DRRs computation process. For each pixel $\mathbf{x}$, the corresponding ray is split into two parts: inside and outside the VOI. The constant outside part is precomputed, and at each iteration only the inside part is integrated and updated to the sum of both parts. The sampling region $\mathrm{S_{VR}}$ contains the projected VOI. We introduce here two object-adaptive sampling regions: (b) the projected object region $\mathrm{S_{OR}}$ and (c) the projected boundary region $\mathrm{S_{BR}}$.

II.C. Strain map computation

A number of mechanical and anatomical parameters can be used to characterize the morphological and dynamic wall properties of the vasculature. We consider the strain map extracted from the non-rigid wall motion estimation as a simplified but adequate way towards characterizing the vascular wall tissue. Such quantities provide a measure of the relative deformation to which the arterial wall is exposed.

We study the distension of the vascular wall, which is related to the changes in wall thickness. This relationship is more evident, for instance, under the volume-preserving assumption as in[3], where the radial Cauchy strain is used. Specifically, it is computed from triangular meshes that are extracted from the estimated volume images. Assuming the volume of the material is preserved, the changes of the area A_{tr} for each triangle are inversely proportional to the changes in wall thickness L_w: $A_{tr} \times L_w = A'_{tr} \times L'_w$. Thus the radial Cauchy strain ε_c is calculated as:

$$\varepsilon_c = \frac{\Delta L_w}{L_w} = \frac{-\Delta A_{tr}}{A'_{tr}}$$

where $\Delta L_w = L'_w - L_w$ and $\Delta A_{tr} = A'_{tr} - A_{tr}$. This means that the strain value is positive if the material is stretched, or negative if it is compressed.

III. VALIDATION

III.A. Experimental data

Our method has been currently applied to cerebrovascular wall motion with a particular emphasis on cerebral aneurysm pulsation. We present here experiments on *in silico* and *in vitro* aneurysm models, and also *in vivo* patient data.

In silico: Twelve cases of digital aneurysm phantom models were created with dome diameters of 8, 10, and 12mm and parent vessel diameter of 4mm. They also have an emerging bleb on the dome. The phantom motion was modeled as smooth geometry changes according to a sinusoidal pulsation waveform and was sampled at a finite number of time points. According to the values on *in vivo* data presented in recent studies[7–9], maximum pulsation amplitudes were set to be 1%-4% of the dome diameter (i.e. 0.08-0.48mm). A sequence of volume images with an isotropic spacing of 0.3mm was generated from the sequence of ground-truth geometries. Voxel intensities were obtained as a function of the signed distance from the voxel to the object surface. The result is an image with a constant value inside the object and another value outside, but with a blurred band of 0.5 mm around the object boundary. Afterwards, this ground-truth volume sequence was used to generate the synthetic measured projections with 0.16mm spacing. In order to simulate other attenuated vessels, air, bones, and soft tissues, we embedded the phantom images into a 3DRA patient image that serves as background. An illustration is shown in Fig. 3(a). Once each phantom was placed within the patient image, the voxels corresponding to aneurysm and vessel were set to a typical intensity value of the CA filled regions.

In addition, in this paper we simulated spurious projection intensity variations in order to analyze the sensitivity of our method and compare with other techniques. Such intensity inhomogeneity is in general caused by the contrast filling following the blood flow. However, the instantaneous local inhomogeneity might be caused by multiple factors. In order to simulate realistic intensity variations, we sampled the RA image intensities from a patient data where the aneurysm dome presented substantial nonuniform intensities including strong blood turbulence. For the phantom dome region in each measured projection, an image patch of the same shape was taken from the dome of the patient case and mapped directly to the phantom image (Fig. 3(b)).

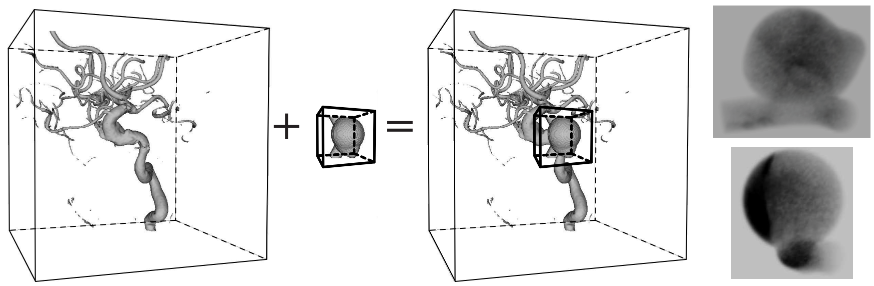

FIG. 3. (a) An example of an *in silico* phantom image, where the phantom model is embedded into a 3DRA patient image. (b) Projections with contrast inhomogeneity synthesized based on a RA patient data with strong blood turbulence.

In vitro: A silicone side-wall aneurysm phantom (Elastrat, Geneva, Switzerland) was used. The model has a spherical dome with 10mm diameter and a straight cylindrical parent vessel with 4mm diameter. It was placed in a rectangular container with dimensions comparable to a human head. The container was water-filled to mimic the attenuation of head tissue. In addition, two other phantoms with straight tubes were also placed in the container to simulate background. The phantom was water-filled and connected to a customized pulsatile pump, a continuous flow pump (Elastrat, Geneva, Switzerland), and a liquid tank to create a continuous and pulsatile flow circuit (Fig. 4(a)).

The image acquisitions were performed using an Allura Xper FD20 scanner (Philips Healthcare, Best, The Netherlands) equipped with a 220mm detector field of view (diagonal dimension) allowing a coverage of 75mm of a cubic volume during a single rotation. For these acquisitions, the injection protocol consisted of 18 mL of iodinated contrast material (Iomeron 400, Bracco Imaging SpA, Milan, Italy) with a flow rate of 3mL/s. RA imaging was performed at a frame rate of 30 Hz during contrast injection, with a 2s delay. These settings of the model and the imaging conditions give a realistic amount of scattering, beam hardening and noise. An example RA image of the *in vitro* phantom is shown in Fig. 4(b). In total, 121 images were acquired (1024^2 pixels with $(0.154\text{mm})^2$/pixel) spanning $\sim 210°$ along the gantry trajectory, from which a 3D volume of 256^3 voxels ($(0.3\text{mm})^3$ per voxel) was reconstructed. X-ray source and detector positions were recorded for each projection, allowing the spatial relationship between the reconstructed reference volume and each projection to be known. The scanning procedure and the imaging parameters of the

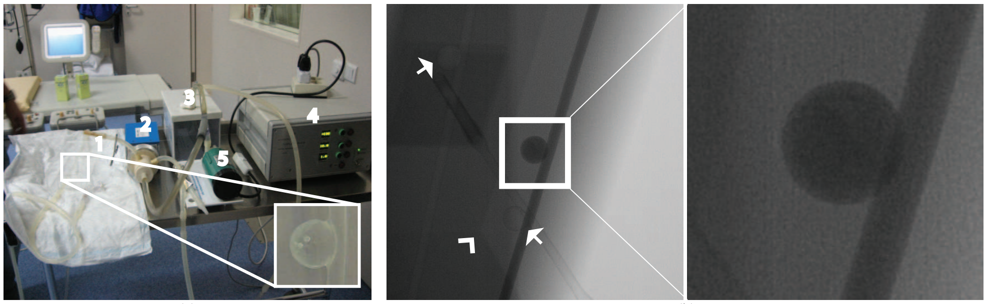

(a) (b)

FIG. 4. (a) *In vitro* phantom experiments setup: 1. the silicone side-wall aneurysm; 2. the customized pulsatile pump; 3. the liquid tank; 4. the pulsatile signal generator; 5. the continuous flow pump. (b) An example X-ray angiography of the *in vitro* phantom. The phantom was placed in a water-filled rectangular container (*arrow head*) with dimensions comparable to a human head. Two additional aneurysm phantoms with straight tubes (*arrows*) were also placed in the container, to act as background.

system followed a standard clinical protocol, which were also used for the *in vivo* cases presented below. Detailed values are summarized in Table. I.

Three acquisitions were performed at different pump piston movement settings, resulting in three phantom pulsation states: large pulsation (LP), small pulsation (SP), and non-pulsation (NP). Although exact aneurysm pulsation amplitudes were unknown, the pulsation range was in accordance with the expected range from visual inspection.

In vivo: Two 3DRA acquisitions from two patients with cerebral aneurysms were analyzed in this paper. Both examinations were collected at Rothschild Foundation Paris, using an Allura Xper FD20 scanner (Philips Healthcare, Best, The Netherlands). For these examinations, the injection protocol consisted of 24 mL of contrast agent (Iomeron 350, Bracco Imaging SpA, Milan, Italy) with a flow rate of 4mL/s, with a 2s delay. Patients were under general anesthesia during the whole examination. We have estimated motion at various locations as indicated in Fig. 5. Three types of motion were visually observed from these regions: aneurysm wall motion, vessel wall motion, and catheter tip displacement. For patient #1, aneurysm motion could not be confirmed from the RA sequence, but we observed it from an available digital subtraction angiography (DSA) sequence. For patient #2, aneurysm motion was not visible in the RA sequence, but we did observe vessel motion and longitudinal displacements of the catheter.

TABLE I. 3DRA imaging settings for the *in vitro* and *in vivo* data, using the Allura FD20 imaging system.

Parameters	**Unit**	**Value**
Tube Voltage	KV	78-89
Tube Current	mA	180-280
Exposure Time	ms	6-8
Detector Dose	nGy/fr	∼200
Detector Format	cm	22, 27
Focal Spot Size	mm	0.4
Source-To-Isocenter Distance	mm	∼810
Source-To-Detector Distance	mm	∼1195
Geometric Magnification	-	∼1.475
Rotation Range	°	∼210
Number of Projections	-	121
Frame Rate	fps	30
Pixel Spacing	mm	0.154
Voxel Spacing	mm	0.3
Contrast Injection Time	s	6
Contrast Injection Rate	mL/s	3-4
Iodine Density	mg/mL	350-400
Collimator Filter (Alu)	mm	1.0
Collimator Filter (Cu)	mm	0.1
Anti-Scatter Grid	lp/cm	80

For all the experiments tested on these data, we chose a VOI of approximately 50^3 voxels. The number of sampled pixels in the sampling regions S_{VR}, S_{OR} and S_{BR} at each projection view were in the order of 5000, 3000 and 500, respectively. The *B*-spline control point grid spacing was about 1.5mm for the spatial dimension, and 10-12.5% of the canonical motion cycle for the temporal dimension.

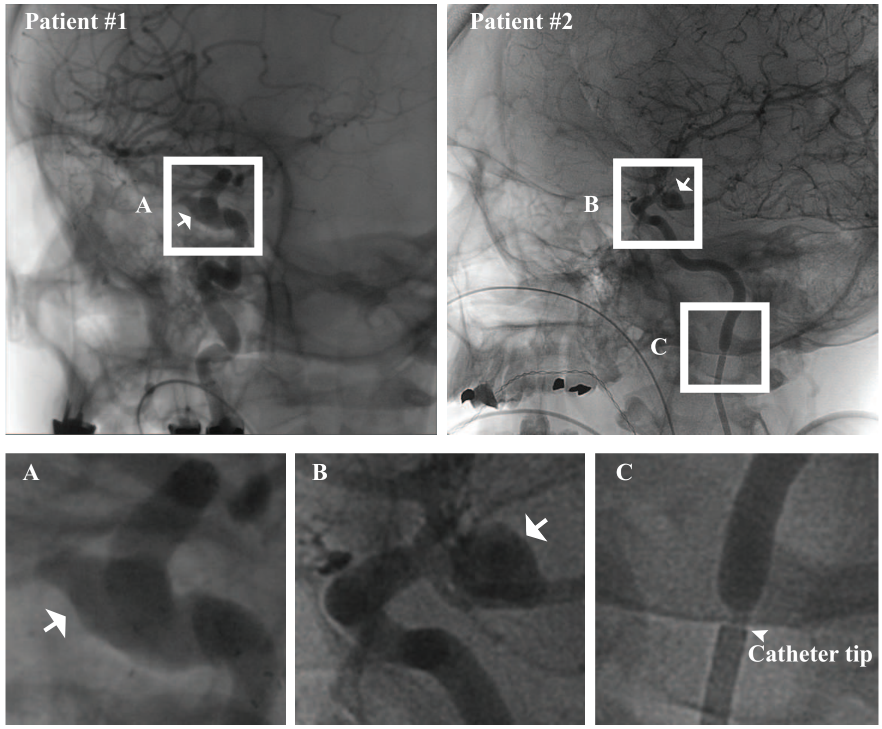

FIG. 5. Details of *in vivo* datasets, indicating with *arrows* the aneurysms and with an *arrow head* the catheter tip. Data from two patients are used in this work, where our method has been applied to different regions: (A) aneurysm with visible motion; (B) aneurysm without visible motion; (C) vessel segment with visible motion, and the imaged catheter (lower part) with longitudinal displacement.

III.B. Accuracy evaluation

In order to quantitatively evaluate the accuracy of the estimated motion, a set of deformed 3D volume images at discrete time points was extracted according to the estimated 4D transformation. A relative error was measured at each time point t as a percentage of the pulsation range,

$$e(t) = \big(m_r(t) - m_g(t)\big)/\hat{m}_g \times 100\%, \tag{4}$$

where $m_g(t)$ is the ground-truth pulsation measurement (e.g., volume changes) at t, $m_r(t)$ the corresponding estimated measurement, and $\hat{m}_g$ the variation range of $m_g(t)$ over the canonical cycle.

In terms of volume change measurements, they were calculated using a method similar

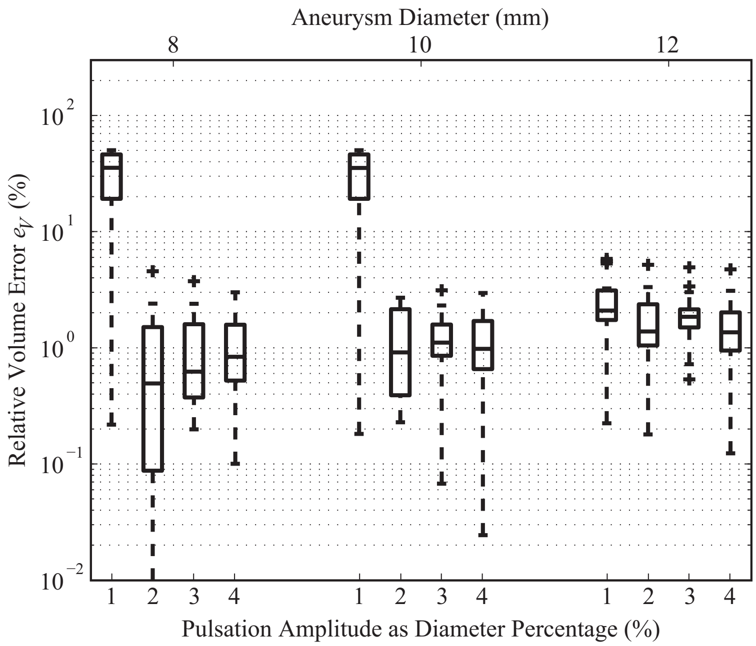

FIG. 6. Boxplots of e_V at 16 equally distributed time points for 12 *in silico* phantom cases of different diameter (8, 10, and 12mm) and maximum pulsation range (1%-4%).

to the one as in[32], by transforming a binary mask image using the deformation field and subsequently summing up the intensities. The partial volume of the boundary voxels was calculated by dividing the sum of the interpolated intensities by the interval length.

IV. RESULTS

IV.A. *In silico* aneurysm wall motion

For each case, we extracted 16 volume images at equally distributed time points along the canonical motion cycle. As the ground-truth is known for these phantom data, a quantitative accuracy evaluation is possible. In the presented experiments, we used the relative error in volume changes, e_V, calculated according to Eq. 4. Except for two cases in which the maximum pulsation was below 0.1mm (being the 8mm and the 10mm dome with 1% maximum pulsation), the relative error in volume changes, e_V, was below 10%, as can be seen in Fig. 6.

In the example shown in Fig. 7, e_V and the computational time are plotted for the same number of registration iterations. In this experiment, we investigated the effects of

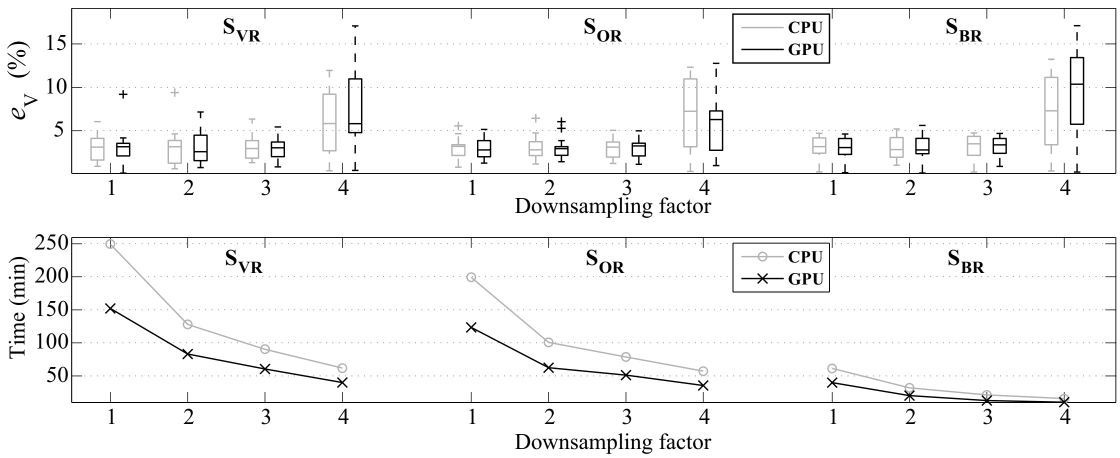

FIG. 7. Performance evaluation on the use of a combination of three different schemes in terms of estimation error e_V and computational time. The three schemes are: sampling regions (S_{VR}, S_{OR}, S_{BR}), angular resolutions along the C-arm gantry trajectory (downsampling factor being 1-4), and the GPU implementation. Results were obtained from an *in silico* phantom with 12mm diameter and 3% pulsation (i.e. maximum amplitude of 0.36mm).

using a combination of three different schemes: sampling region, angular resolution along the C-arm gantry trajectory, and the GPU implementation. The angular resolution of the measured projection sequence was downsampled by a factor of 1 to 4. Results show similar accuracy ($e_V < 5\%$ up to three quartiles) achieved from the three sampling regions combined with an angular resolution downsampling factor up to 3. Therefore, given the fact that less projections can be used, it can be speculated that this also enables discarding the use of a few undesirable projections, e.g. the ones with severe artifacts. No significant differences were obtained when DRRs were generated using either the CPU or GPU implementation. The slight GPU/CPU discrepancies can be attributed to the difference in data type specifications between the processors[33]. Due to the speedup introduced at the GPU-based DRR generation stage, the image registration process can be reduced by an additional factor of up to 2x with respect to the corresponding CPU-based implementation. Therefore, the estimation results for the complete motion cycle can be obtained in 5-10 minutes when using S_{BR} on the GPU DRR implementation using a downsampling factor of 3.

Fig. 8 shows the color maps of the amplitude wall displacements and the radial Cauchy strain estimated at the maximum and minimum pulsation states of an *in silico* phantom

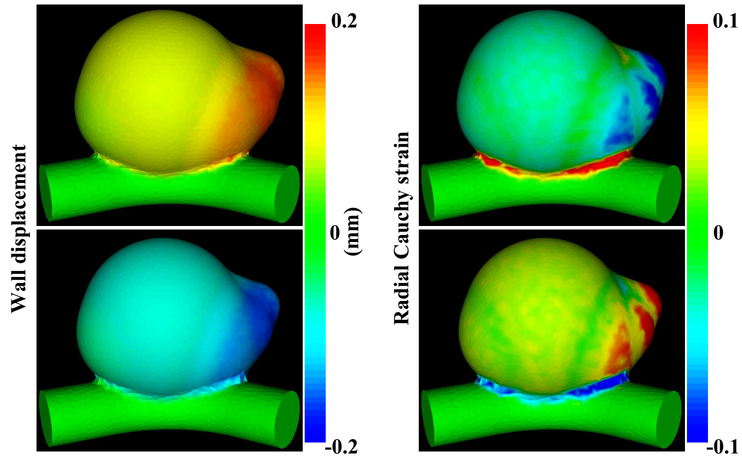

FIG. 8. Wall displacement amplitude and radial Cauchy strain at the maximum (*top*) and minimum (*bottom*) deformation states for an *in silico* phantom with diameter of 12mm and pulsation of 3% (i.e. maximum amplitude of 0.36mm).

with diameter of 12mm and pulsation of 3% (i.e. maximum amplitude of 0.36mm). In regions with similar surface curvatures like the dome, the strain field presents a similar pattern to the displacement field, whereas in regions with higher curvatures, such as the bleb and the neck, the strain scales faster. This suggests that the strain field might enhance more efficiently regions having a different deformation pattern as strain is less insensitive to passive motion but focuses on differential motion.

IV.B. *In vitro* aneurysm wall motion

For the three pulsation states under evaluation, we obtained larger motion in the LP case, smaller motion but with a similar pattern in the case of SP, and no motion for the NP case. We show here the results of the LP case in Fig. 9. As the ground-truth is unknown, the results are qualitatively presented. In Fig. 9(a-b), a measured projection is compared with its corresponding DRRs calculated from the reference volume and from our estimated volume. From the visual inspection in the projection space, our technique demonstrates its ability in correcting the misalignment between the measured projection and the DRR. In Fig. 9(c-d), color maps show the wall displacement amplitude and the strain at the time point with the largest motion. An inhomogeneous wall displacement distribution is observed and is especially concentrated on a lateral side of the aneurysm dome. This is caused by a

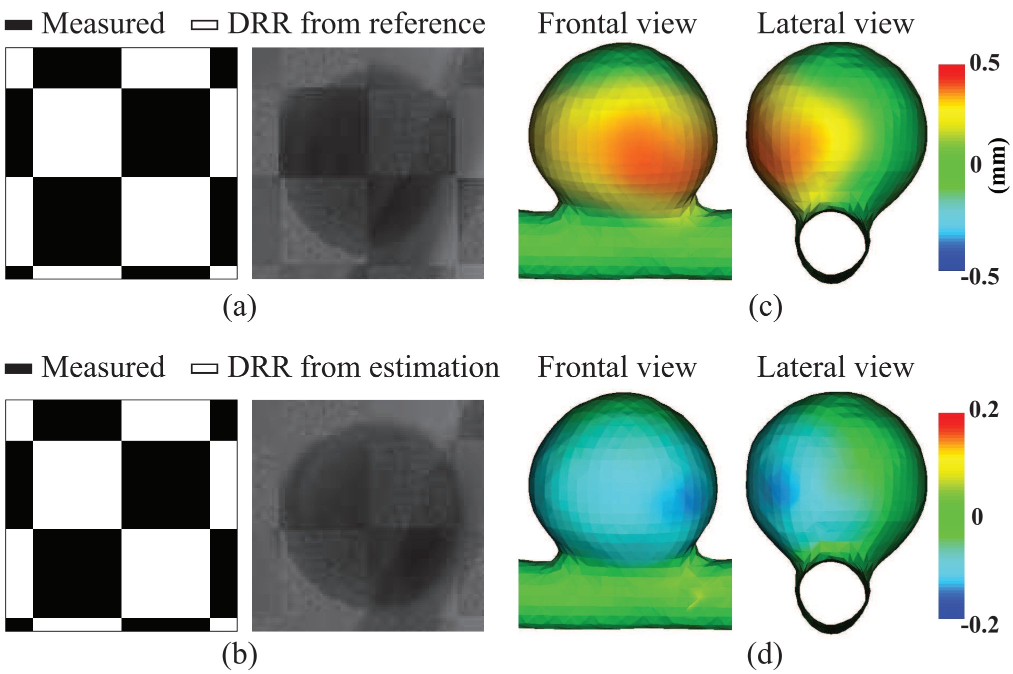

FIG. 9. Results from *in vitro* LP phantom: (a,b) Example of checkerboard images for the *in vitro* phantom comparing respectively the measured projection with the equivalent DRR computed from the reference volume and our estimation. The color maps of the wall displacement amplitude (c) and the radial Cauchy strain (d) for the frontal and lateral views at the instant presenting the largest displacement.

slight axial tilting of the phantom tube position during the acquisition. This is in agreement with the reduced effect in terms of strain distribution observed at the same location, since part of the displacements came from a global movement.

IV.C. *In vivo* cerebrovascular motion

Our estimation recovered the visually observed aneurysm motion from patient #1 and vessel motion from patient #2. For patient #2, aneurysm motion was neither observed nor recovered. Fig. 10 and Fig. 11 summarize the recovered motion from patients #1 and #2, respectively. The color maps show the displacements and the radial Cauchy strain at the end-systolic (ES) phase, which coincided with the cardiac time of the measured projections where maximum motion was visually observed. This phase represented also the time of the maximum motion estimated from our technique, as can be seen in the displacement curves

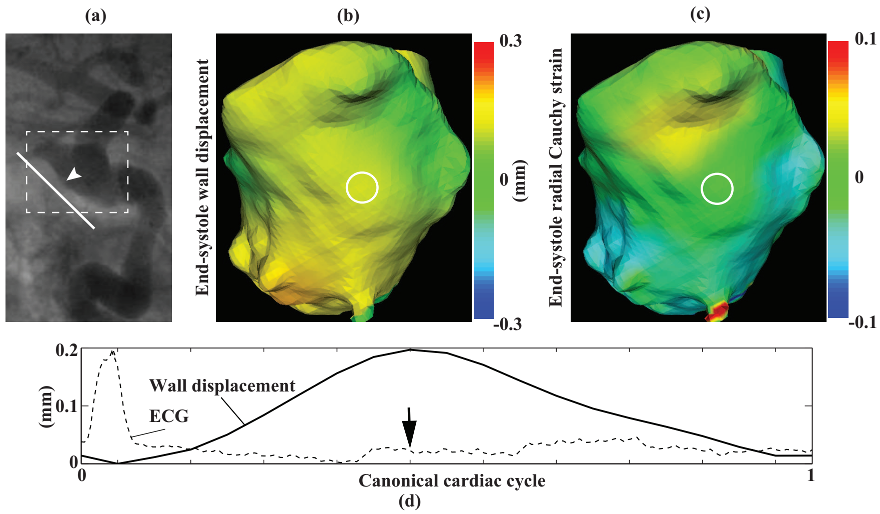

FIG. 10. Results of aneurysm wall motion in patient #1. (a) A close view indicating the region where our motion estimation method has been applied (*dashed frame*) in an X-ray angiography. (b) The color map (*line* in (a) indicating the viewing plane) of the displacements around the end-systolic (ES) phase (indicated by the *arrow* in (d)). (c) The radial Cauchy strain at the same phase as in (b). (d) Aneurysm wall displacement amplitude over the cardiac cycle at the location indicated by the *arrow head* in (a) and the *circles* in (b,c).

over time in both figures. These curves show that the aneurysm in patient #1 and the vessel motion in patient #2 presented a similar pattern with respect to the cardiac phases indicated by the ECG signal. Spatially, for instance in Fig. 10, the motion was clearly observed in the projections only in a small area of the aneurysm dome, which coincides with the maximum estimated wall displacement region using our technique. Also, we observed that, in Fig. 11 the upper part of the vessel (i.e. internal carotid artery) did not show any visible motion. This is consistent with the fact that this particular vessel segment, i.e. the petrous segment, is surrounded by stiff bony structures preventing any motion at this location.

IV.D. Catheter displacement

From the measured projections for patient #2, we observed substantial longitudinal displacement of the catheter, corresponding to the catheter tip moving vertically along the direction of the vessel and following the blood flow. To further verify the feasibility of our method in recovering general motion other than vascular wall motion from a rotational

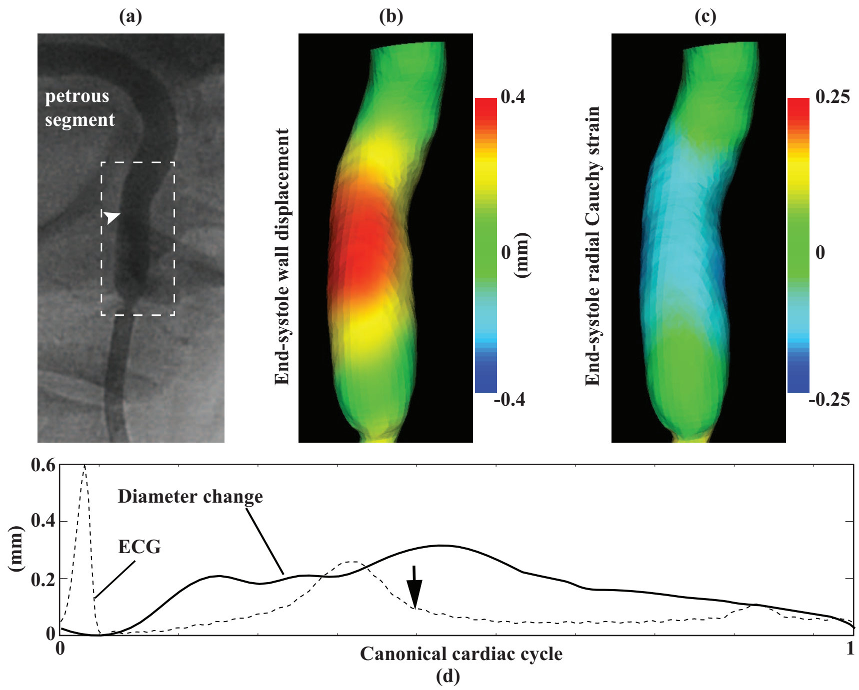

FIG. 11. Results of vessel wall motion in patient #2. (a) A close view indicating the region where our motion estimation method has been applied (*dashed frame*) in an X-ray angiography. (b) The color map of the displacements around the end-systolic (ES) phase (indicated by the *arrow* in (d)). (c) The radial Cauchy strain at the same phase as in (b). (d) The vessel diameter change over the cardiac cycle at the location as indicated by the *arrow head* in (a).

angiography acquisition, we have applied it to the imaged catheter region and recovered the displacement of the catheter tip. Results are shown in Fig. 12. The color maps show respectively the displacements (Fig. 12(a)) at 10 equally sampled time instants over the cardiac cycle. And the catheter tip displacement (along the vessel longitudinal direction) is plotted with the ECG signal in Fig. 12(c). The cardiac phase when the maximum value of this movement occurred was similar to the maximum vessel motion phase (Fig. 11(d)). This confirms that the catheter moved back and forth according to the pulse of the blood flow. We have also plotted the calculated strain maps at the catheter surface in Fig. 12(b). As the strain represents deformation instead of rigid movement, it should be ideally zero everywhere and for all time instants. As expected, at the lower and homogeneous part of the catheter, zero radial displacements and strain values were obtained. However, they were not zero everywhere at the catheter tip. A first explanation for such behavior of the results is

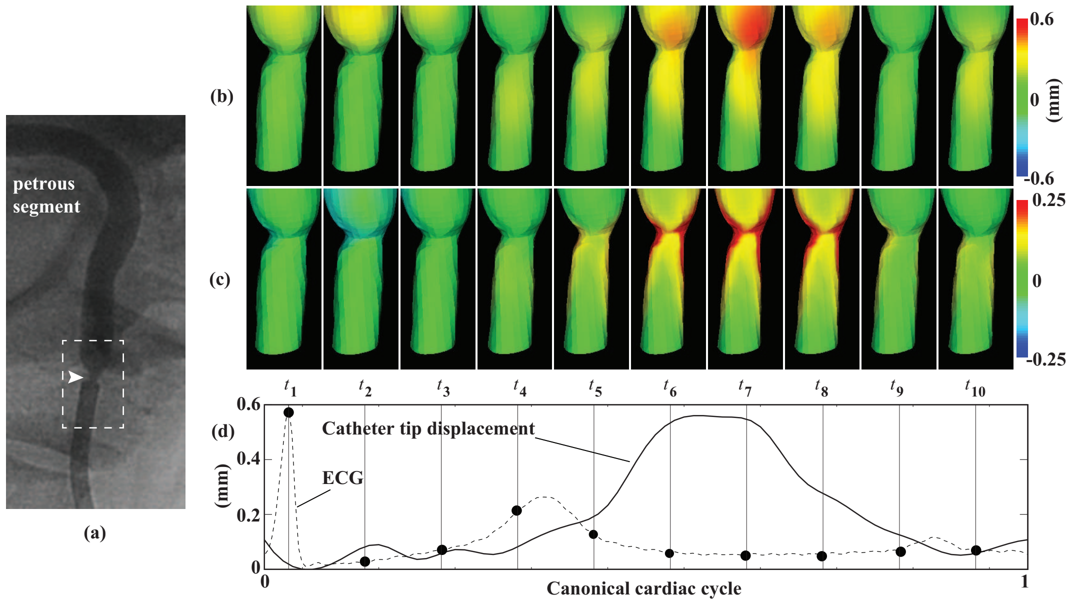

FIG. 12. Results of catheter tip movements in patient #2. (a) A close view indicating the region where our motion estimation method has been applied (dashed frame) in an X-ray angiography. The color maps of the estimated catheter movements (b) and the strain (c) at ten selected time points. (d) The catheter tip (arrow head in (a)) longitudinal displacement plotted together with the ECG signal.

that the catheter used during the intervention had a flexible tip and therefore was prone to deformation. Second, the estimated vessel motion was "propagated" to its immediate vicinity, the catheter tip, since the B-spline transformation provides a spatially smooth estimate of the displacement field. And third, at the catheter tip, larger inhomogeneity of the contrast agent mixing are expected, which in turn might affect our intensity-based registration method.

V. DISCUSSION

In silico pulsatile aneurysm phantom results have demonstrated that the estimation error was below 10% in recovering motion in the sub-millimeter range, e.g. in the order of a voxel, even from images with substantial intensity inhomogeneity. *In vitro* aneurysm phantom experiments have allowed verifying that our method is able to detect whether an aneurysm pulsates or not. However, in a clinical environment, due to the lack of ground-truth motion information, we were not able to validate quantitatively the performance of the method. Nonetheless and for the first time, experiments carried out on *in vivo* patient data presenting visible aneurysm and vascular wall motion as well as catheter tip movement, have demonstrated the feasibility of our method for motion detection and recovery from RA. In regions where motion or deformation is impossible from an anatomical point of view, such as the petrous segment and the catheter, the results were consistent with the expected zero motion. In summary, although ground-truth was unknown for the *in vitro* and the *in vivo* data, our results were qualitatively accurate. Given the realistic modeling of spatial and temporal imaging conditions as well as the morphology and motion range, the performance of our method on *in silico* data can be expected, **to a certain extent, to be translatable** to patient data acquired in a clinical situation.

To facilitate the translation of this technique into clinical practice, we proposed the joint use of two acceleration strategies together with their implementation on graphics processing units. This has demonstrated a successful memory management and speedup for processing large 3D and 2D datasets from 3DRA acquisitions. These improvements allowed completing the motion estimation process for one entire cycle in 5-10 minutes without degrading the overall performance. More specifically, we obtained a 3-4x speedup from the precomputation of surrounding vascular structures outside the VOI, and a 10x from the use of S_{BR}. With respect to the CPU implementation, an additional speed improvement of up to 2x was achieved by integrating the GPU generated DRRs in the motion estimation framework.

Since the object-adaptive ROIs are calculated based on two selected voxel values as described in Section II.B.2, the potential influence of these intensity values on the estimation is discussed here. Experiments were performed on an *in silico* phantom (dome diameter of 12mm and maximum pulsation of 3%) embedded in a 3DRA patient image. Voxel intensities of the phantom dome were set to be constant inside (i.e. a value belonging to the CA filled region), and to be smoothly changing on the boundary, depending on the distance from the voxel to the ideal wall surface. Results are demonstrated on four S_{BR} regions (denoted as R1-R4), chosen from different combinations of four sub-ranges equally spanning the intensity range of the phantom. The lower boundary intensity value of R1 was chosen to be higher than the actual boundary and thus was inside the phantom. That means, in R1 the aneurysm wall was not included, while in R2 to R4 the actual aneurysm wall was always included but with the inner boundary identified by three different values spanning the aneurysm intensity

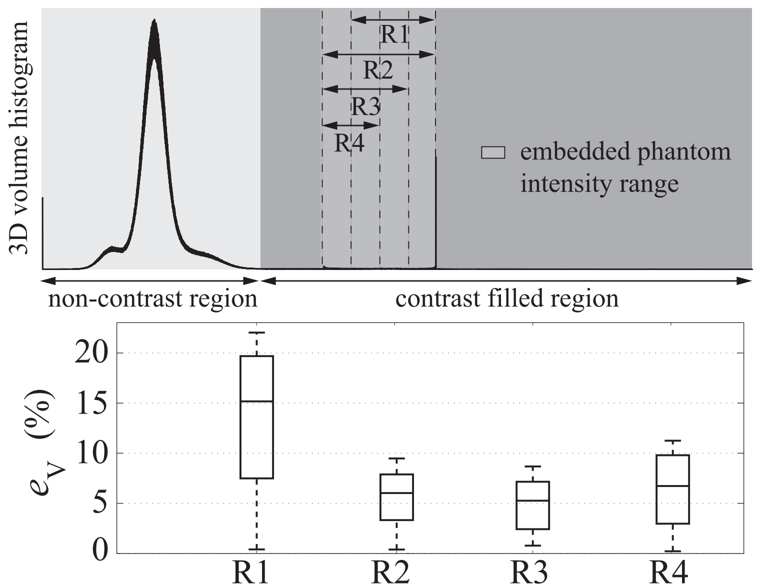

FIG. 13. Comparison of the accuracy using four different S_{BR} regions (denoted as R1-R4), chosen from different combinations of four sub-ranges equally spanning the intensity range of the phantom. Results in this figure were obtained from an *in silico* phantom embedded in a 3DRA patient image (see an illustration in Fig. 3(a)). The phantom has a diameter of 12mm and the maximum pulsation of 3% (i.e. maximum amplitude of 0.36mm).

range. Detailed distributions of these four regions are illustrated on the histogram of the reference volume image, as shown in Fig. 13. Their corresponding relative estimation error e_V values are also plotted in the figure. Results suggest that the choice of the voxel intensity values for the boundary region does not affect much the estimation accuracy, when the expected wall motion region is within the chosen S_{BR}. In the case of R1, larger errors were obtained because this region excludes the intensity range of the aneurysm wall by focusing on too high intensities.

In the following, we discuss the performance comparison between a previous technique[18] for 3D independent motion estimation at specific time points (denoted as ALG1) and our proposed 4D motion cycle estimation technique (denoted as ALG2). In general, similar accuracy values could be expected using both techniques, since the plot shown in Fig. 7 presented comparable error values as reported in[18]. In terms of computational efficiency, the time spent for a full 4D motion estimation in this paper is comparable to what is needed for computing only one 3D estimation at a specific time point using ALG1. In the

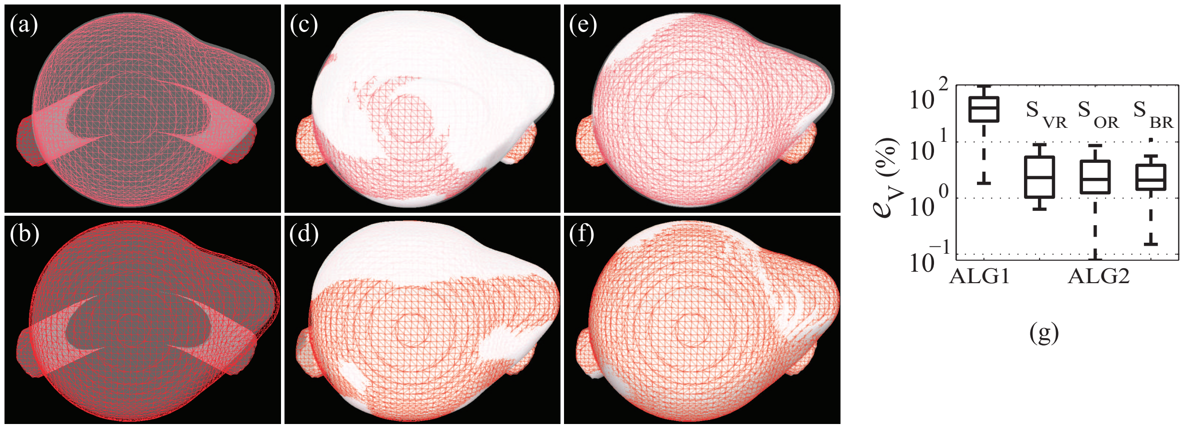

FIG. 14. Results comparing the influence of inhomogeneous contrast filling on the method in[18] (denoted as ALG1) and our present technique (denoted as ALG2), using an *in silico* phantom with diameter of 10mm and pulsation of 4% (i.e. maximum amplitude of 0.4mm). Results at two instants are shown graphically: (a,c,e) minimum pulsation and (b,d,f) maximum pulsation. The ground-truth shape (wireframe representation) at each time instant is overlaid with: (a,b) the reference, (c,d) the estimation using ALG1, and (e,d) the estimation using ALG2. (g) Comparison of e_V between ALG1 and ALG2 with the three sampling regions: $\mathrm{S_{VR}}$, $\mathrm{S_{OR}}$, and $\mathrm{S_{BR}}$.

situation with large intensity variations in the contrast-enhanced regions in the projection images, such as inhomogeneous contrast mixing, our method or ALG2 is however expected to be more robust than ALG1. Results shown in Fig. 14 were obtained from the simulated inhomogeneous contrast-filled images, as described in Section III.A. The relative volume error e_V was below 10% using ALG2, whereas using ALG1 it was on average 50% or even larger. This large difference is due to the fact that ALG1 failed to recover the motion from such input images. This can be visually observed in Fig. 14 from the surface of the ground-truth shapes at two example time instants overlaid with the estimations (i.e. maximum and minimum shape extension). Constrast inhomogeneity in this case induces an overestimation of the phantom motion using ALG1 in comparison with ALG2. This suggests that our 4D estimation is more robust to large image intensity inhomogeneity, both temporally and spatially. Additionally, a slightly higher accuracy was obtained using the projected boundary region $\mathrm{S_{BR}}$. This could be possibly due to the exclusion of inner regions with inhomogeneous intensities, reducing the noise influence to the registration.

As the expected cerebral aneurysm wall motion range is very small, the impact of other possible physiological motion that might affect the motion estimation needs to be discussed. The most intuitive one is respiratory motion, however in our application its impact is negligible. First, from the clinical examination protocol point of view, the respiratory induced motion in the head is not likely to happen, given that the patient lies still, either under general anesthesia **or when instructed to hold their breath** for a few seconds during the 3DRA acquisition (in our case 4s), with the head in an immobilizing headrest. Second, from our methodology point of view, we use projections from one canonical cardiac cycle that are built from multiple cardiac cycles, and we model this cycle by a 4D smooth and continuous transformation. The method assumes pseudo-periodicity in such a way that acts as a filter forcing the reconstructed motion to be just one canonical cycle. This, in effect, helps to reinforce motion induced by blood pressure changes occurring over the cardiac cycle, and meanwhile, produces an averaging of other physiological motion that does not occur with the cardiac cycle, such as respiratory motion. In fact, it works in a similar way as how standard 3DRA reconstructions ignore the existence of any kind of motion. This reference reconstruction is reliable because the potential motion is small in comparison with the size of the reconstructed objects. In our case, the estimated pseudo-periodic vascular motion should be reliable while the spontaneous irregular non-periodic motion is small in comparison with the periodic motion. These reasons can also justify the ignorance to the possible irregular variation (or large deviations) of the cardiac cycles. Recently, after following over 30 cerebral aneurysm embolization interventions we have found an intrascan heart beat variability below 1.5% on average and not exceeding 4%. This variability is small enough to be averaged or compensated by our method. Other movements throughout the rotational run that might also have an influence is related to highly attenuated structures, e.g. bones or the skull. In this case, the possibility and the amount of this motion variation are negligible, as the bone movement can be considered to be global and very small. Specifically because the skull is covering all the imaged region, and its material and motion can be assumed to be homogeneous. Furthermore, this effect is minimal under our methodology framework, since the ray traverses through a highly contrast-enhanced object, and the projection intensity is mostly determined by the accumulated attenuation of the contrast-enhanced vessels. Therefore, the potential projection intensity variation caused by the movement of bones for a specific projection pixel can be ignored in principle. This also confirms that our acceleration strategy, the precomputation outside the region of interest is a reliable approximation. However, in the case **that a substantial amount** of any of the aforementioned motion occurs during the acquisition, the reliability of the estimated vascular motion could be decreased.

In general for X-ray imaging applications, the variations of intrinsic detector performance parameters could probably play a role in the image quality, as has been studied intensively in[34–39]. These parameters can provide characteristics that consider the complete imaging system performance, including the effect of focal spot blurring, magnification and scatter. They have more pronounced effects for general applications with less image contrast[34] or small structures like stent struts (e.g. 0.1mm or lower)[35,37] using a microangiographic fluoroscopic imaging system[37,38]. In our case, the studied objects like selective CA enhanced vascular structures are imaged with high dose and are highly contrasted. Also object size is expected to be in a larger magnitude. Admittedly, the intrinsic spatial extent of the detector limits the motion recovering of our technique to a certain range. But the use of a sparse set of B-spline control points means that the estimated motion of each control point is determined by many points along the object surface and boundary. This enables us to obtain a realistic estimation of the wall motion whose magnitude is equivalent to small fractions of the total system mean imaging aperture or unsharpness. Meanwhile, note that this limited resolution **of currently existing systems** is expected to be improved in the future, which will enable our method to estimate even smaller motion. This factor is reflected in the results shown in Fig. 6 on *in silico* phantom experiments. In this figure, at least for two phantom cases (8mm and 10mm with 1% motion for both), we were not able to recover correctly the motion. Further resolution improvements and thus motion estimation with small magnitude could be expected when geometric unsharpness effects can be minimized either through reduction of the focal spot size or reduction of the magnification. However, the options for a reduction of the aforementioned two factors are limited. As this study serves to show the feasibility of 4D aneurysm wall motion estimation from rotational angiography, a more detailed analysis of the impact of these factors on the estimation accuracy and robustness will be addressed in future work and is beyond the scope of this paper.

The experimental results also emphasize the feasibility of performing strain analysis from the estimated motion, making thus possible the use of this information for further estimating elastic properties of the vascular wall, using for example an inverse problem approach[3]. Note that the strain map was not obtained through tracking individual points or tissue on the vascular wall. Thus, our approach for strain calculation through quantifying apparent motion from images implies that the correspondences over time are approximations of the same physical point.

VI. CONCLUSIONS

This paper has presented a technique to recover 4D cerebrovascular wall motion that is in the order of sub-millimeter, from a single 3DRA acquisition within a clinically acceptable computation time. Using this technique, the recovered motion is temporally and spatially smooth, which also improves the robustness of the estimation to noise and intensity inhomogeneity. The subsequent strain calculation based on our motion estimation provides further progress towards the biomechanical modeling of the cerebrovascular wall. Our technique also provides the possibility of detecting vascular wall abnormalities through direct visualization of motion over time. It is highly desirable to have a technique that offers accurate and robust *in vivo* estimates of such motion. In order to translate **our method into a clinical setting**, future research efforts should be paid to validate our method on a **larger number of patient data sets.**

ACKNOWLEDGMENTS

The authors would like to thank Dr. Raphaël Blanc from Rothschild Foundation Paris, for the patient data acquisitions, Dr. D. Rüfenacht and L. Augsburger from Geneva University Hospitals, for providing the aneurysm silicone phantom and the pulsatile pump, J.-M. Dhieux and J.-P. Ruaud from Philips France for their technical support, and R. Hermans from Philips Healthcare (Best, The Netherlands) for 3DRA data software. They also thank R. Cárdenes for the helpful discussion. This work was partially supported by the CENIT-CDTEAM grant funded by the Spanish Ministry of Science and Innovation, partially generated in the framework of the @neurIST Integrated Project, which is co-financed by the European Commission (IST-027703), and partially supported by the Spanish Ministry of Science and Innovation (Ref. TIN2009-14536-C02-01), Plan E and FEDER.

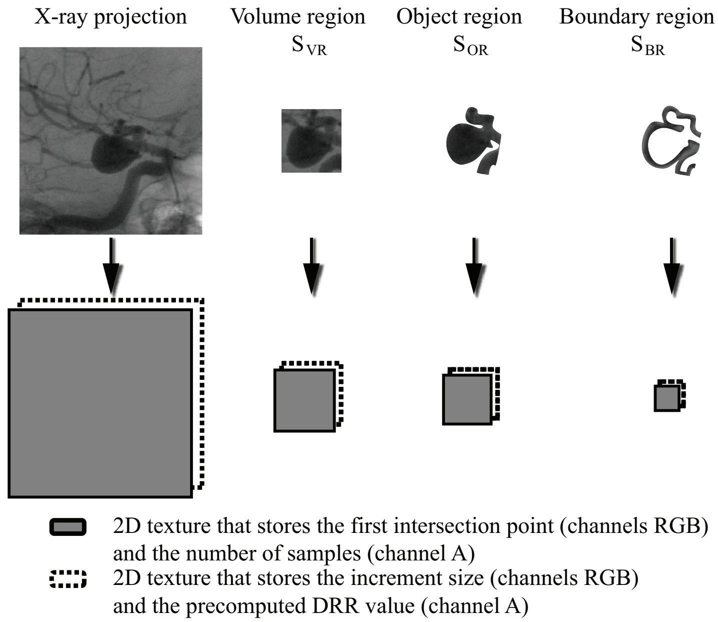

FIG. 15. An illustration of how information is repacked for the final DRRs computation for the proposed three structures of interest (S_{VR}, S_{OR} and S_{BR}) into 2D textures of decreasing sizes.

Appendix: GPU implementation of DRRs generation

To further speedup the method, the DRRs generation combined with the acceleration strategies is implemented on GPU and is integrated into the image registration process. We briefly describe the main idea of the method here. Unlike traditional GPU-based DRR generation methods[40], our implementation also integrates the two previously introduced strategies, thus benefits from both the GPU parallelization and the resultant memory reduction from these strategies.

The method was implemented using the Cg (C for graphics) toolkit[41] and on the pixel shader units of a NVIDIA GeForce 8600 GT graphics card with 512MB of memory, hosted by an Intel ® Core™2 Quad CPU Q6600 2.40GHz with 4GB of memory. DRR pixel data are stored as stream data in the format of textures, and fed to the GPU fragment units so that each fragment works in parallel on a single pixel. Each texture element can store up to four components, or the RGBA channels, as they are originally used to represent the red, green, blue, and alpha intensities of a color for rendering. In order to reduce redundant calculations, we compute first a number of parameters that are constant when updating the DRRs during each iteration. As we equidistantly sample points on the ray (Fig. 2(a)), only the first intersection point on the volume and the sampling step vector are needed, the remaining points can be derived in a straightforward manner. In total, eight constant parameters are needed for each pixel to calculate the DRRs: the first intersection point, the sampling step, the number of sampled points and the pre-computed DRR value. Since we only calculate the pixel values within the ROIs (S_{VR}, S_{OR}, or S_{BR}), these eight constant parameters to calculate the pixel values in the ROI are re-packed into two 2D rectangular textures of smaller sizes than the original projections (see an illustration in Fig. 15). They are used in a GPU procedure that only performs the main loop over the VOI at every registration iteration. This way, the GPU fragment code remains short to maintain the stream processing advantage with respect to its equivalent CPU calculations.

REFERENCES

[1] D. M. Sforza, C. M. Putman, and J. R. Cebral, "Hemodynamics of cerebral aneurysms," Annu. Rev. Fluid. Mech. **41**, 91–107 (2009).

[2] J. C. Lasheras, "The biomechanics of arterial aneurysms," Annu. Rev. Fluid. Mech. **39**, 293–319 (2007).

[3] S. Balocco, O. Camara, E. Vivas, T. Sola, L. Guimaraens, H. A. F. Gratama van Adel, C. B. Majoie, J. M. Pozo, B. H. Bijnens, and A. F. Frangi, "Feasibility of estimating regional mechanical properties of cerebral aneurysms in vivo," Med. Phys. **37**, 1689–1706 (2010).

[4] M. Kroon and G. A. Holzapfel, "Estimation of the distributions of anisotropic, elastic properties and wall stresses of saccular cerebral aneurysms by inverse analysis," Proc. R. Soc. A **464**, 807–825 (2008).

[5] L. Dempere-Marco, E. Oubel, M. Castro, C. Putman, A. F. Frangi, and J. R. Cebral, "CFD analysis incorporating the influence of wall motion: application to intracranial aneurysms," in *R. Larsen, M. Nielsen, and J. Sporring (Eds.): MICCAI2006, LNCS4191* (2006) pp. 438–445.

[6] F. Ishida, H. Ogawa, T. Simizu, T. Kojima, and W. Taki, "Visualizing the dynamics of cerebral aneurysms with four-dimensional computed tomographic angiography," Neurosurgery **57**, 460–471 (2005).

[7] T. Krings, P. Willems, J. Barfett, M. Ellis, N. Hinojosa, J. Blobel, and S. Geibprasert, "Pulsatility of an intracavernous aneurysm demonstrated by dynamic 320-detector row

CTA at high temporal resolution," Cent. Eur. Neurosurg. **70**, 214–218 (2009).

[8]C. Karmonik, O. Diaz, R. Grossman, and R. Klucznik, "In-vivo quantification of wall motion in cerebral aneurysms from 2D cine phase contrast magnetic resonance images," Rofo. **182**, 140–150 (2010).

[9]E. Oubel, J. R. Cebral, M. DeCraene, R. Blanc, J. Blasco, J. Macho, C. M. Putman, and A. F. Frangi, "Wall motion estimation in intracranial aneurysms," Physiol. Meas. **31**, 1119–1135 (2010).

[10]V. Rasche, B. Movassaghi, M. Grass, D. Schäfer, and A. Bücker, "Automatic selection of the optimal cardiac phase for gated three-dimensional coronary x-ray angiography," Acad. Radiol. **13**, 630–640 (2006).

[11]D. Schäfer, J. Börgert, V. Rasche, and M. Grass, "Motion-compensated and gated cone beam filtered back-projection for 3-D rotational X-ray angiography," IEEE Trans. Med. Imag. **25**, 898–906 (2006).

[12]B. Movassaghi, M. Grass, D. Schaefer, V. Rasche, O. Wink, G. Schoonenberg, J. Y. Chen, J. A. Garcia, B. M. Groves, J. C. Messenger, and J. D. Carroll, "4D coronary artery reconstruction based on retrospectively gated rotational angiography: first in-human results," in *Proc. SPIE Med. Imag.: Visualization and Image-Guided Procedures*, Vol. 6509 (2007) p. 65090P.

[13]C. Blondel, G. Malandain, R. Vaillant, and N. Ayache, "Reconstruction of coronary arteries from a single rotational X-ray projection sequence," IEEE Trans. Med. Imag. **25**, 653–663 (2006).

[14]L. A. Feldkamp, L. C. Davis, and J. W. Kress, "Practical cone beam algorithms," J. Opt. Soc. Am. A **6**, 612–619 (1984).

[15]C. Rohkohl, G. Lauritsch, L. Biller, M. Prümmer, J. Boese, and J. Hornegger, "Interventional 4D motion estimation and reconstruction of cardiac vasculature without motion periodicity assumption," Med. Image Anal. **14**, 687–694 (2010).

[16]R. Zeng, J. A. Fessler, and J. M. Balter, "Estimating 3-D respiratory motion from orbiting views by tomographic image registration," IEEE Trans. Med. Imag. **26**, 153–163 (2007).

[17]J. Vandemeulebroucke, J. Kybic, P. Clarysse, and D. Sarrut, "Respiratory motion estimation from cone-beam projections using a prior model," in *G.-Z. Yang et al. (Eds.): MICCAI2009, LNCS5762* (2009) pp. 365–372.

[18]C. Zhang, M.-C. Villa-Uriol, M. De Craene, J. M. Pozo, and A. F. Frangi, "Morphody-

namic analysis of cerebral aneurysm pulsation from time-resolved rotational angiography," IEEE Trans. Med. Imag. **28**, 1105–1116 (2009).

[19]C. Zhang, M. De Craene, M.-C. Villa-Uriol, J. M. Pozo, B. H. Bijnens, and A. F. Frangi, "Estimating continuous 4D wall motion of cerebral aneurysms from 3D rotational angiography," in *G.-Z. Yang et al. (Eds.): MICCAI2009, LNCS5761* (2009) pp. 140–147.

[20]C. Zhang, M.-C. Villa-Uriol, and A. F. Frangi, "Evaluation of an efficient GPU implementation of digitally reconstructed radiographs in 3D/2D image registration," in *Proc. SPIE Med. Imag.: Image Processing* (2010) p. 762333.

[21]M. Unser, "Splines: a perfect fit for signal and image processing," IEEE Signal Process. Mag. **16**, 22–38 (1999).

[22]D. Rueckert, L. I. Sonoda, C. Hayes, D. L. G. Hill, M. O. Leach, and D. J. Hawkes, "Non-rigid registration using free-form deformations: application to breast MR images," IEEE Trans. Med. Imag. **18**, 712–721 (1999).

[23]R. L. Siddon, "Fast calculation of the exact radiological path for a three-dimensional CT array," Med. Phys. **12**, 252–255 (1985).

[24]P. Viola and W. M. Wells, "Alignment by maximization of mutual information," Int. J. Comput. Vision **24**, 137–154 (1997).

[25]F. Maes, A. Collignon, D. Vandermeulen, G. Marchal, and P. Suetens, "Multimodality image registration by maximization of mutual information," IEEE Trans. Med. Imag. **16**, 187–198 (1997).

[26]D. Mattes, D. R. Haynor, H. Vesselle, T. K. Lewellen, and W. Eubank, "PET-CT image registration in the chest using free-form deformation," IEEE Trans. Med. Imag. **22**, 120–128 (2003).

[27]C. Zhu, R. H. Byrd, and J. Nocedal, "L-BFGS-B: Algorithm 778: L-BFGS-B, FORTRAN routines for large scale bound constrained optimization," ACM Trans. Math. Software **23**, 550–560 (1997).

[28]M. R. Sabuncu and P. J. Ramadge, "Gradient based nonuniform subsampling for information-theoretic alignment methods," in *Proc. Int. Conf. IEEE Eng. Med. Biol. Soc.*, Vol. 3 (2004) pp. 1683–1686.

[29]R. Bhagalia, J. A. Fessler, and B. Kim, "Accelerated nonrigid intensity-based image registration using importance sampling," IEEE Trans. Med. Imag. **28**, 1208–1216 (2009).

[30]H. Bogunović, A. G. Radaelli, M. DeCraene, D. Delgado, and A. F. Frangi, "Image

intensity standardization in 3D rotational angiography and its application to vascular segmentation," in *Proc. SPIE Med. Imag.: Image Processing* (2008) p. 691419.

[31]N. Otsu, "A threshold selection method from gray-level histograms," IEEE Trans. Syst. Man. Cybern **9**, 62–66 (1979).

[32]M. Holden, J. A. Schnabel, and D. L. G. Hill, "Quantification of small cerebral ventricular volume changes in treated growth hormone patients using nonrigid registration," IEEE Trans. Med. Imag. **21**, 1292–1201 (2002).

[33]IEEE, "IEEE standard for floating-point arithmetic," IEEE Std 754-2008 , 1–58 (2008).

[34]V. Rasche, B. Schreiber, C. Graeff, T. Istel, H. Schomberg, M. Grass, R. Koppe, E. Klotz, and G. Rose, "Performance of image intensifier-equipped X-ray systems for three-dimensional imaging," in *Proc. CARS, Computer Assisted Radiology and Surgery*, Vol. 1256 (2003) pp. 187–192.

[35]I. S. Kyprianou, S. Rudin, D. R. Bednarek, and K. R. Hoffmann, "Generalizing the MTF and DQE to include x-ray scatter and unsharpness: Application to a new microangiographic system," Med. Phys. **32**, 613–626 (2005).

[36]G. K. Yadava, I. S. Kyprianou, S. Rudin, D. R. Bednarek, and K. R. Hoffmann, "Generalized two-dimensional (2D) linear system analysis metrics (GMTF, GDQE) for digital radiography systems including the effect of focal spot, magnification, scatter, and detector characteristics," in *Proc. SPIE Med. Imag.: Physics of Medical Imaging*, Vol. 5745 (2005) pp. 419–429.

[37]V. Patel, K. R. Hoffmann, C. N. Ionita, C. Keleshis, D. R. Bednarek, and S. Rudin, "Rotational micro-CT using a clinical C-arm angiography gantry." Med. Phys. **35**, 4757–4764 (2008).

[38]G. K. Yadava, S. Rudin, A. T. Kuhls-Gilcrist, and D. R. Bednarek, "Generalized objective performance assessment of a new high-sensitivity microangiographic fluoroscopic (HSMAF) imaging system," in *Proc. Soc. Photo Opt. Instrum. Eng.* (2008) p. 69130U.

[39]A. Jain, A. T. Kuhls-Gilcrist, S. K. Gupta, D. R. Bednarek, and S. Rudin, "Generalized two-dimensional (2D) linear system analysis metrics (GMTF, GDQE) for digital radiography systems including the effect of focal spot, magnification, scatter, and detector characteristics," in *Proc. SPIE Med. Imag.: Physics of Medical Imaging* (2010) p. 76220K.

[40]P. Després, J. Rinkel, B. Hasegawa, and S. Prevrhal, "Stream processors: a new platform for Monte Carlo calculations," in *Journal of Physics: Conference Series, Third McGill*

International Workshop, Vol. 102, edited by F. Verhaegen (2008) p. 012007.

[41] W. R. Mark, R. S. Glanville, K. Akeley, and M. J. Kilgard, "Cg: A system for programming graphics hardware in a C-like language," ACM Trans. Graphics **22**, 896–907 (2003).